Analysis of Fracture Mechanics Tests on Opalinus Clay

Analysis of Fracture Mechanics Tests on Opalinus Clay

S. Valente[1], C. Fidelibus[2], S. Loew[3], M. Cravero[4], G. Iabichino[5] and F. Barpi[6]

[1]Department of Structural Engineering and Geotechnics, Politecnico di Torino, Italy
Tel.: +39-011-0904853, Fax: +39-011-0904899, *silvio.valente@polito.it*

[2]Institute of Environmental Geology and Geoengineering, National Research Council of Italy, Torino, Italy

[3]Department of Earth Sciences, ETH Zurich, Switzerland

[4]Institute of Environmental Geology and Geoengineering, National Research Council of Italy, Torino, Italy

[5]Institute of Environmental Geology and Geoengineering, National Research Council of Italy, Torino, Italy

[6]Department of Structural Engineering and Geotechnics, Politecnico di Torino, Italy

Keywords Anisotropy, Cohesive crack, Opalinus Clay, SCB test

Abstract *Many studies have recently been conducted to evaluate various mechanical characteristics of the Opalinus Clay (OPA) formation in view of its potential use as the hosting rock for the Swiss nuclear waste repositories. Its sedimentary bedding makes OPA a transversely isotropic rock and its directional mechanical properties need to be measured. This paper reports on an experimental and computational approach that was adopted to define the parallel-to-bedding Fracture Mechanics (FM) parameters of OPA in Mode-I. OPA cores from Mont Terri Underground Research Laboratory (URL) were submitted to laboratory tests on notched Semi-Circular specimens under three-point Bending (SCB). In these tests, crack propagation is forced along the notch direction. However, the 45° bedding inclination of the specimen axis frequently deviated the crack from the expected direction. An analysis of the SCB tests was performed by means of non-linear FM techniques and the pertinent Mode-I parameters along the bedding were estimated.*

1 Introduction

Opalinus Clay (OPA) is a tight clay shale that is considered a good candidate to host the Swiss nuclear waste repositories for low/intermediate and high level wastes, because of its high compaction and very low permeability. However, excavation-induced disturbances are produced around the periphery of a gallery or cavern in this rock at a depth of 300-900m below the ground surface, that is, at the repository depth. Because of several factors, including: depth, in-situ stress state, gallery orientation, shape and size, excavation method, air moisture, water saturation and local mechanical properties of rock, existing fractures are reactivated and new fractures of variable size may form, thus compromising the integrity of the rock mass in a relatively small zone around the gallery, called the Excavation Damaged Zone (EDZ). These fractures may be connected along the direction of the gallery axis and give rise to an increase in the rock mass permeability along the same direction. A model of the rock mass in which these fractures are explicitly included might be required for the analysis of the radionuclide transport around the gallery (Hudson et al (2009)). Therefore, there is a need to clearly understand the crack growth process in such a material in the framework of a Fracture Mechanics (FM) approach. The FM parameters of the OPA need to be measured in order to simulate this process.

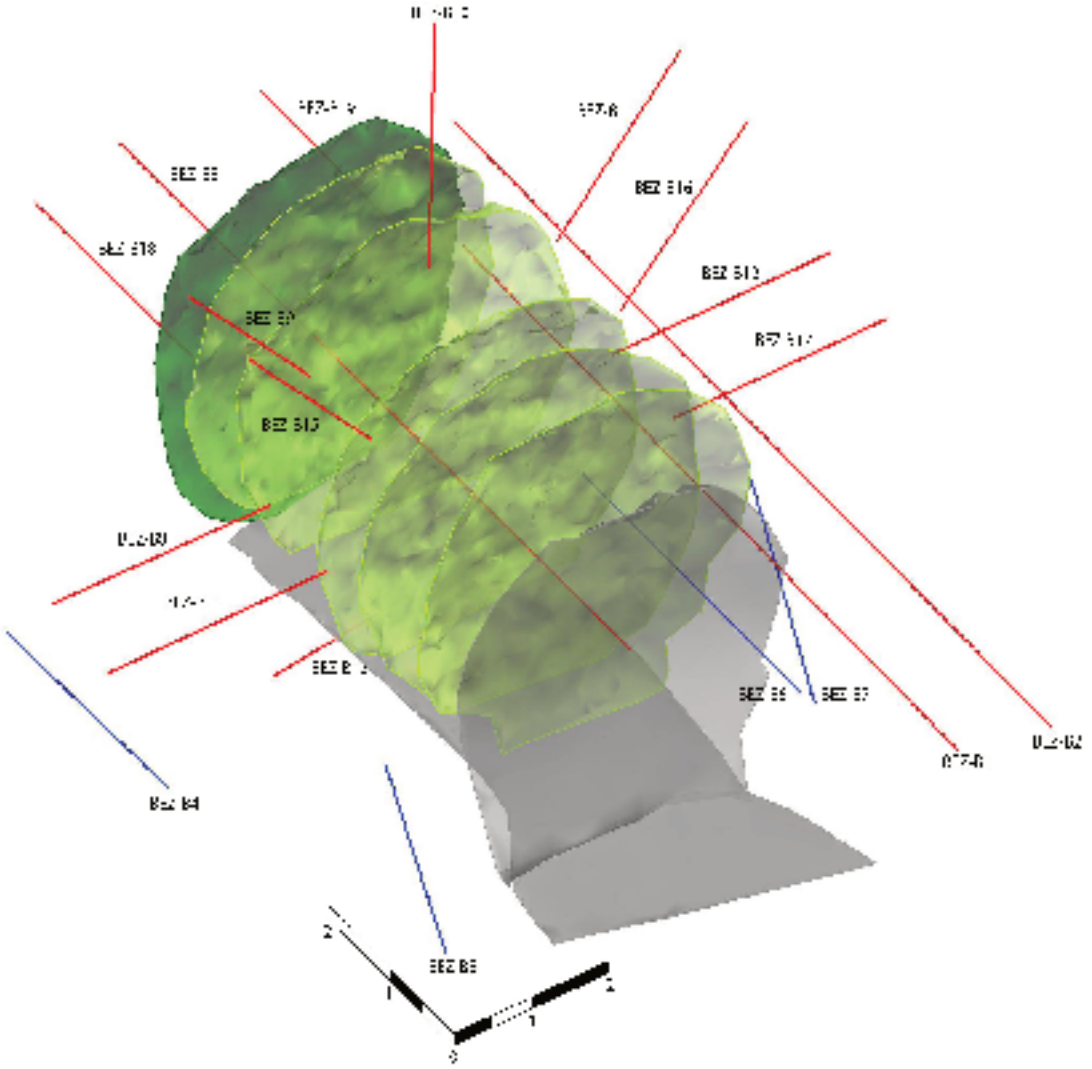

Figure 1: An isometric view of the EZ-B niche and its boreholes. The first face in grey is that of the entrance, the next five faces in yellow are the intermediary ones and the last one in green is the final face. The pore pressure boreholes are shown in blue and the observation boreholes are in red. The top of the concrete floor is shown in grey (after Yong et al (2006)).

The Chair of Engineering Geology at ETH Zurich, in cooperation with the Swiss Nuclear Safety

Inspectorate ENSI, designed and successfully conducted the EZ-B mine-by experiment in the Mont Terri URL. The experiment was aimed at mapping and modelling EDZ fractures around a niche (or test gallery, 3.8m in diameter and 6.5m in length), excavated in multiple stages (Yong et al (2006), Yong (2007), Yong et al (2010)). Fracture traces on the niche walls were carefully mapped and several observation boreholes were executed from inside the niche (see Figure 1). The longitudinal and the vertical boreholes intercepted the bedding of the clay shale with an angle of approximately 45°. Specimens from the longitudinal boreholes were subjected to specific FM tests at the rock mechanics lab of the Institute of Environmental Geology and Geoengineering, National Research Council of Italy, in Turin.

Because of the bedding, OPA can be considered a transversely isotropic geo-material with planes of isotropy that coincide with the bedding planes (Bock (2001)). The FM parameters of the OPA are orientation-dependent. SCB tests were performed to measure the FM parameters along the bedding, and the results were interpreted by resorting to Non-Linear Elastic Fracture Mechanics (NLFM). The NLFM application required the use of a Finite Element Method (FEM) code.

In this paper, the test results and interpretations are documented, after a description of the general geological/geomechanical properties of the OPA and the crack growth features in the OPA EDZ. Finally, the concluding remarks are given.

2 OPA mineralogy, structure and strength

Opalinus Clay was deposited 180 million years ago in a shallow basinal marine environment (Wetzel and Allia (2003)). The estimated maximum burial depth occurred during the Cretaceous and Miocene eras and reached about 1000m at Mont Terri (Mazurek (2002)). Opalinus Clay is a dark grey shale that consists of claystone and marl with intercalated sandy and calcareous layers and lenses. The shaly facies at Mont Terri is composed of 58–76% clay particles, essentially kaolinite and illite, 0-28% of carbonates, and 6-24% of quartz (Gaucher et al (2003)). There are no signs of calcite crystals in the SEM images, indicating that the calcite is amorphous and a source of cementation (Corkum and Martin (2007)). The bedding in the Opalinus Clay consists of persistent, millimetric spaced layers with varying clay minerals, quartz and calcite contents. The sedimentary heterogeneities include shell fragments and pyrite crystals (up to 1mm), and larger siderite concretions and sandy nodules.

Three main persistent sets of mm-thick tectonic shears and one major thrust zone were mapped in the Mont Terri URL (Nussbaum et al (2011)). The most frequent set is oriented parallel to the bedding, underwent only small shear displacements of the order of millimeters and self-sealed with clay minerals and calcite.

The rock mechanics properties of cores, sampled at various orientations with respect to the bedding have been investigated by many researchers. The most recent compressive strength tests focused on macroscopic extensional fracturing at low confining stresses (i.e. around excavations), and are presented in Amann et al (2011). Their experiments were performed approximately normal to the bedding, at natural water contents, and showed an average UCS of 6.9MPa, a crack initiation threshold of about 30%, and a crack damage threshold of 70% of UCS. The crack initiation and crack damage thresholds correspond to the lower and upper limits of the in-situ strength relevant for extensional fracturing in the EDZ.

When defining the OPA strength parameters, one should consider that the OPA composition, texture and structure show differentiation and heterogeneities at the micro scale. These natural intrinsic differentiations of the sedimentary rock implicitly influence the behavior of the OPA, as can be seen from the variability of the results obtained from various types of mechanical laboratory tests.

3 Crack growth in EDZ

3.1 EDZ fracturing in homogeneous and isotropic rock

The safety of a deep nuclear waste repository may be enhanced if appropriate countermeasures are undertaken in order to reduce the amount of fracturing produced in the vicinity of the tunnel walls

after the excavation. Chandler (2004) showed that adopting a non-circular shape can hamper the generation of cracks and help preserve the integrity of the material after excavation.

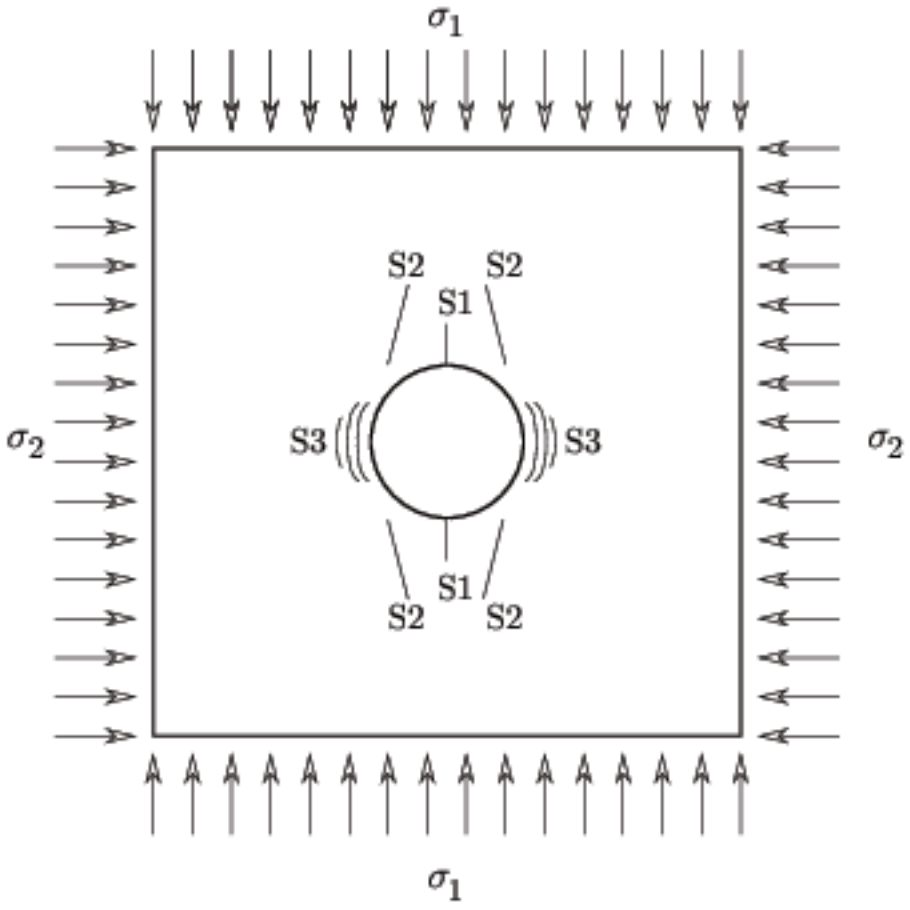

Figure 2: Fractures emanating from a circular hole; S1 primary fractures, S2 remote fractures, S3 sidewall fractures (after Carter et al (1992))

The damage and fracturing processes around a hole in homogeneous rock has been extensively investigated (see e.g. Chandler (2004), Ewy and Cook (1990),Germanovich and Dyskin (2000), Hajiabdolmajid et al (2002)). Carter et al (1992) claimed that, in a homogeneous and isotropic medium, there are three sets of fractures which may emanate from a cavity: *primary*, *remote* and *sidewall* fractures (Figure 2). Primary fractures are the first to form and they align along the direction of the maximum principal vertical stress σ_1 (compressive stresses positive here). The initiation of these fractures may incur when $\sigma_1 > f_t + 3\sigma_2$, where f_t is the rock tensile strength. These primary fractures are extensional and determine a stress re-distribution which in turn promotes the growth of the remote fractures. These fractures initiate close to the extremities of the primary fractures and propagate in a slanted direction with respect to the direction of σ_1. These two fracture sets do not necessarily appear.

A third set is constituted of the sidewall spalling fractures, which grow almost parallel to the sidewall and the maximum principal stress direction. These fractures can be considered evidence of a compressive failure at low confinement. With reference to Figure 3, if unconstrained, these fractures may subsequently buckle and form tension cracks. If the depth of spalling is sufficient to create a notch-like damage zone, the failure mode within the rock can transit to dilational shear at the notch tip and create additional bulking (Diederichs (2007)). Such notchlike damage zones are considered to be critical for the safety of nuclear waste repositories under adverse stress conditions (e.g. Chandler (2004)).

The term 'compressive' refers to the macroscopic scale; at a micro scale, these fractures are in fact mainly tensile fractures that propagate from pre-existing flaws or defects (micro-cracks, pores, stiffer concretions). This type of failure at the sidewall can be explained in the framework of a micromechanical approach, where FM concepts are applicable. As the excavation progresses, the deviatoric

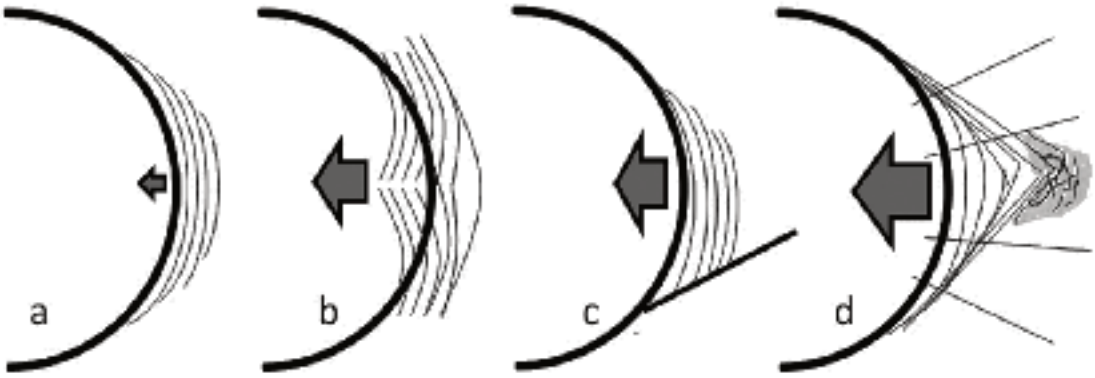

Figure 3: Progressive development of sidewall spalling, buckling and tensile fracturing of sidewall spalls, and notch formation (after Loew et al (2010))

stress and stress ratios increase, giving rise to some micro-cracks that propagate in a stable manner; this implies that only the decrease in confinement can sustain the propagation. Whether this process leads to a macroscopic failure or not depends above all on the 3D stress path and rock damage at the tunnel face, the stress levels and ratios behind the tunnel face, the pre-failure rock mechanics properties, and the tunnel geometry (Diederichs (2007)).

As shown hereafter, the EDZ in the Mont Terri URL shows much more complex fracturing patterns that have been extensively investigated by several research groups. The above-described conceptual model for homogeneous isotropic rock needs to be further developed for the OPA considering the rock mass heterogeneities and anisotropy.

3.2 EDZ in the anisotropic and heterogeneous clay shale at Mont Terri

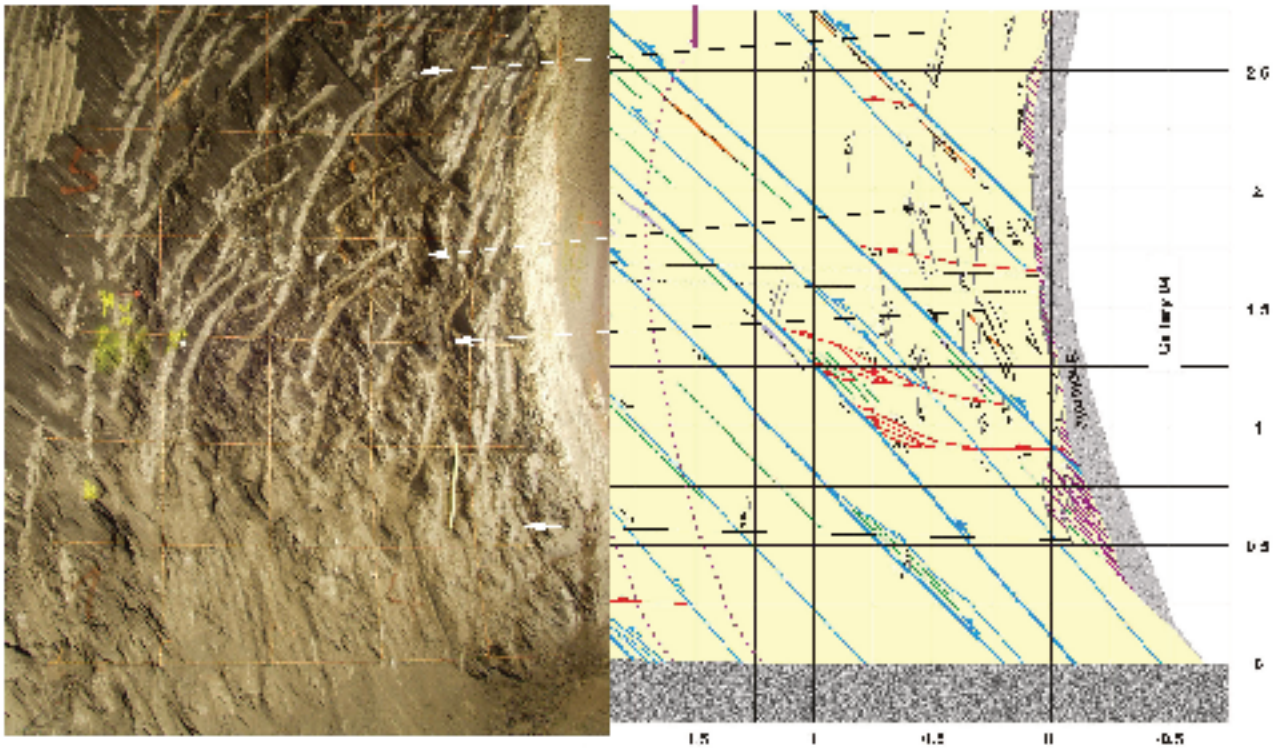

Figure 4: Mapped EDZ fractures in the East wall of entrance to the EZ-B niche (after Yong et al (2006)). Left: photo of niche entrance with striations from hydraulic hammer, mapping grid, and weak traces of tectonic faults and EDZ fractures(white arrows). Right: detailed map of same location, showing tectonic shear fractures in blue and red, EDZ fractures (in black) and reactivated bedding planes in purple. Bedding is marked with green lines.

The macroscopic fracturing around the excavation at Mont Terri has been investigated and classified by Thury and Bossart (1999), Nussbaum et al (2011), Martin and Lanyon (2001) and Yong et al (2006, 2010). The EDZ at Mont Terri extends for half to one tunnel radius in the OPA formation and consists of reactivated tectonic fractures, bedding planes, and sidewall fractures that strike parallel and are inclined to the gallery axis (see the example in Figure 4). The progressive formation of the EDZ around a short test tunnel, with a diameter similar to a high-level waste drift, has been explored in detail by Yong (2007). This so-called EZ-B field experiment is described in detail in Yong et al (2006) and Yong et al (2010). With reference to Figure 4, in the EZ-B test tunnel, located in the shaly facies of the Opalinus Clay, the bedding has a dip of about 45° (in the opposite direction to the tunnel axis) and only two main sets of tectonic shears are identified. The dominant set consists of metric-spaced parallel-to-bedding shears, the secondary set consists of sub-horizontal shears that are isolated in two areas of the test tunnel, and both have a thickness of only a few millimeters. These shears were reactivated at the intersection of the EZ-B test tunnel with the main gallery during excavation; the local stress fields were modified and this caused the formation of new EDZ fractures that primarily grew normal to the reactivated bedding planes or parallel to the excavation walls.

Numerical analyses have shown that after mobilization of the tectonic shears, the stress levels in the matrix led to extensional fracturing (spalling). The depth and size of the spalling type fracturing at the sidewalls of the EZ-B test tunnel could be related to changes in the ratio between the minimum and maximum principal stresses (i.e. the spalling limits) as the excavation boundary is approached (Yong (2007)).

Several observations of EDZ fracturing around the Mont Terri URL galleries suggest that a substantial portion of the excavation-induced fractures is oriented along the bedding. Thus, the need

for an assessment of the orientation-dependent FM parameters, in view of the application of a micro-mechanical approach to simulate the EDZ discrete fractures in the Opalinus Clay.

4 Fracture Mechanics of anisotropic materials

The crack growth in geo-materials can be analyzed in the framework of FM, by assuming a linear or a non-linear response of the material in the vicinity of a crack tip.

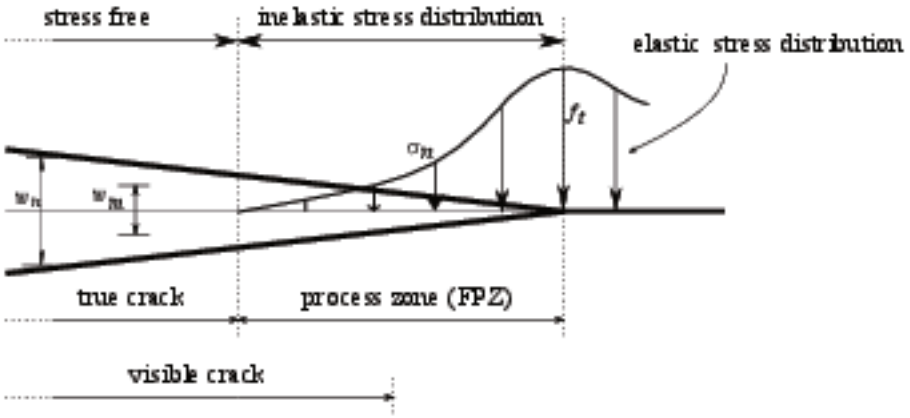

Figure 5: Schematic of the crack tip and fracture process zone according to CCM

Linear Elastic Fracture Mechanics (LEFM) works well when the plastic zone at the tip of a crack is negligible, as occurs in metals or granite. However, the plastic zone in OPA clay is relatively large (compared to the crack). The so-called *Cohesive Crack Model* (CCM) was introduced in the framework of NLFM (Barenblatt (1959), Dugdale (1960), Hillerborg et al (1976), Bocca et al (1991), Barpi and Valente (2010)) to perform the simulation of crack growth under the aforementioned conditions.

According to the CCM, when the principal tensile stress reaches the ultimate tensile strength f_t of the material, the crack is assumed to extend further. Through this extension a normal stress is transferred; its entity is functionally related to the cumulated displacement w_n of the crack walls (the *displacement discontinuity*). In Figure 5, the point in which the non-linear response begins is the *fictitious crack tip*, whereas the point at which w_n reaches a critical value w_m is the *real crack tip*. No stress transfer occurs beyond the latter point and the crack is stress free. The portion of the crack between the real and the fictitious tip is called *Fracture Process Zone* (FPZ).

The FM properties in an transversely isotropic material like the OPA are orientation dependent. Tensile strength is as follows (Buczek and Herakovich (1985)):

$$f_t(\theta) = f_{t\|b}\cos^2(\theta) + f_{t\perp b}\sin^2(\theta) \tag{1}$$

where $f_{t\|b}$ and $f_{t\perp b}$ are the parallel-to-bedding tensile strength and normal-to-bedding tensile strength (both principal values), respectively. Angle θ represents the angle from the bedding plane. In addition, the direction of propagation may differ from the case of an isotropic material and does not necessarily coincide with the direction in which the maximum circumferential stress around the crack tip is active (Saouma et al (1987)).

The results of SCB tests have been interpreted by means of NLFM to obtain the parallel-to-bedding FM parameters, as shown hereafter.

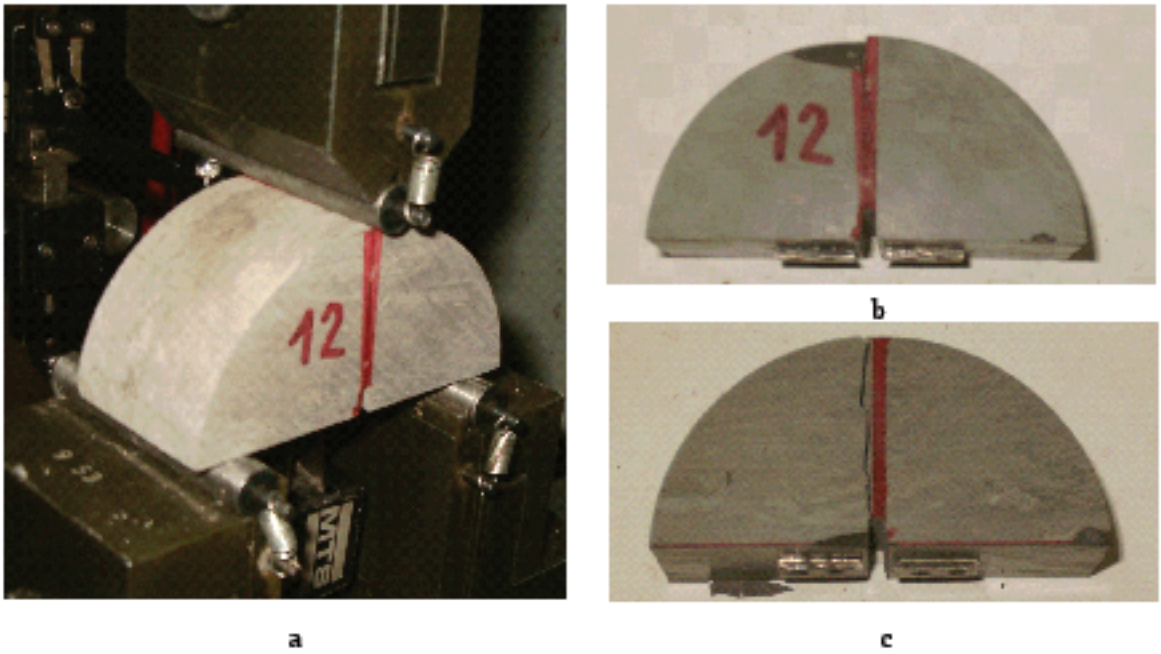

Figure 6: Snapshots of specimen B1912: a) specimen under loading, b) frontal view after failure, c) back view after failure

5 Three-point bending experiments on Opalinus Clay

The laboratory tests for the EZ-B experiment were aimed at defining the FM parameters of the OPA. Given the inherent heterogeneity of the intact rock, the need to conduct a sufficient number of tests in spite of the limited amount of material available. The SCB test is specified for core-based cylindrical specimens; the amount of material required for each test is minimal: a semi-slice of the core of only a few centimeters. It was selected for the EZ-B tests mainly for this reason. In addition, SCB offers other distinctive features: the specimen preparation time is short and the setting up of the equipment is easy. A specimen is obtained by cutting a few cm thick slice of the core and then cutting it into two halves. A notch is then machined from the centre of the circle. After the specimen is placed on two rollers, the loading machine applies a load P to the top up to the failure (see Figure 6). A clip gauge extensometer measures the *Crack Mouth Opening Displacement* (CMOD), i.e. the opening of the notch at the centre of the circle. The vertical displacement (deflection η) can also be monitored at the outer end of the notch. Some of the SCB tests on specimens from the EZ-B niche were run at a constant deflection rate ($0.4 \div 0.6 \mu$/s), while some others were run at a constant CMOD rate ($0.03 \div 0.05 \mu$/s).

In this configuration, considering the orientation of the bedding, with respect to the borehole axis (for all the boreholes), the SCB tests provided the FM parameters of the OPA along the bedding (i.e., the ultimate tensile strength $f_{t\,||b}$, critical displacement discontinuity $w_{m||b}$ and fracture energy $G_{f||b}$) for NLFM. A set of 22 specimens was utilized, 15 specimens from EB-Z B19 and 7 from boreholes B01, B02 and B03. These boreholes also intercepted the bedding at an angle of 45°. The depth of the locations and dimensional characteristics of the specimens are given in Table 1. The geometrical setup of the specimens and bedding planes are reported in Figure 7 .

specimen	x	D	H	S	W	a_0	b_0
B0104		82.5	38.5	38.6	250.32	5.6	2.0
B0105		82.5	39.1	38.6	237.25	5.5	2.0
B0201	8.65-9.03	82.5	39.7	35.0	223.52	4.2	2.0
B0302	7.57-7.78	82.6	39.6	44.8	296.54	5.7	2.0
B0203	-	82.0	37.6	39.7	242.32	4.70	2.0
B0304	7.57-7.78	82.3	39.8	39.1	218.80	5.1	2.0
B0305	7.57-7.78	81.7	39.9	43.8	265.28	6.0	2.0
B1906	0.15-0.28	79.6	38.2	47.5	280.55	7.1	2.5
B1907	0.15-0.28	79.6	38.3	47.7	276.68	7.3	2.8
B1908	0.28-0.40	79.4	37.9	23.4	134.22	6.3	2.5
B1909	0.28-0.40	79.4	38.1	23.4	134.48	6.0	2.4
B1910	0.40-0.50	79.6	38.3	43.1	256.47	5.0	2.3
B1911	0.50-0.60	79.6	38.4	43.1	253.06	5.3	2.0
B1912	0.85-0.92	79.5	37.6	37.9	212.44	5.5	2.3
B1913	0.92-1.00	79.6	39.4	38.0	226.41	6.0	2.1
B1915	1.08-1.16	79.4	39.2	35.7	195.70	5.4	2.6
B1916	1.16-1.30	79.6	38.2	44.3	252.52	6.1	2.2
B1917	1.30-1.50	79.7	39.1	43.1	257.81	5.6	2.1
B1918	1.70-1.90	79.6	39.3	41.0	243.74	5.8	2.3
B1919	1.90-2.17	79.5	37.9	41.2	231.45	6.0	2.3
B1920	2.17-2.27	79.3	37.5	36.2	203.88	6.4	2.2
B1921	2.27-2.37	79.5	39.3	36.2	215.40	7.0	2.2

Table 1: List of the specimens; x[m] distance from the top of the borehole, D[mm] diameter of the core, H[mm] semi-circular specimen height, S[mm] thickness, W[g] weight, a_0[mm] notch depth, b_0[mm] notch width (the support span L[mm] is always 62mm). The first three letters of the specimen label refer to the borehole number (B01, B02, B03, B19)

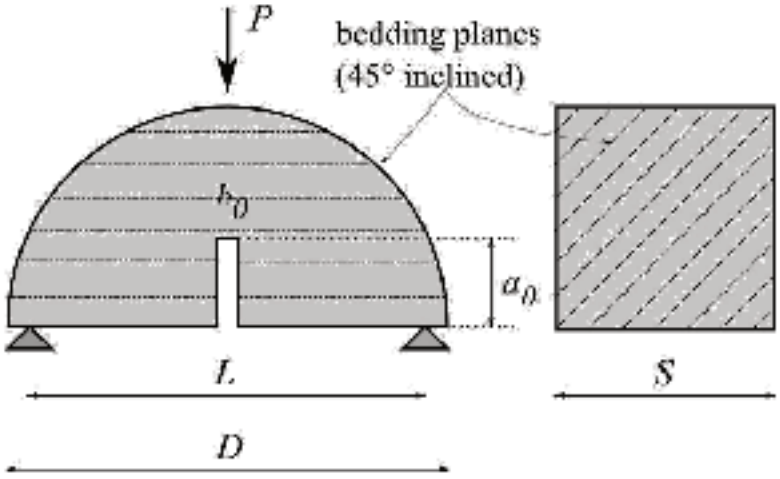

Figure 7: Frontal and lateral views of a specimen subjected to the SCB test and the bedding planes

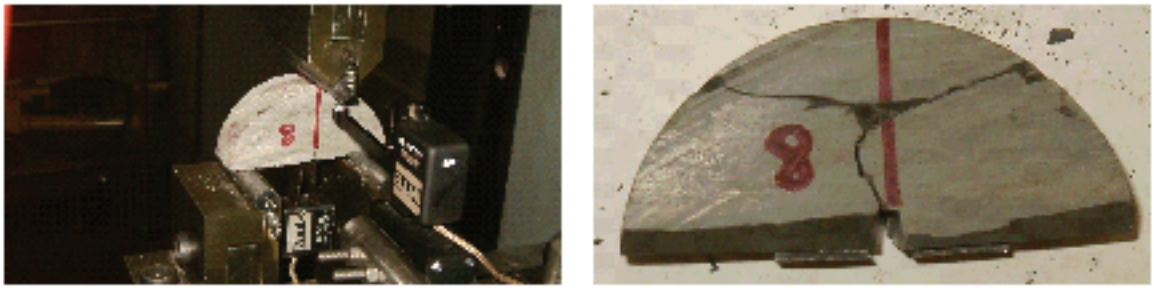

Figure 8: Snapshots of specimen B1908: a) specimen under loading, b) frontal view after failure; the divertion of the crack that initially generated from the notch is evident.

Considering the boundary and load conditions of the test, it is possible to assume that isotropic materials would break following the notch plane. Nevertheless, given the arrangement of the bedding, with respect to the notch, cracks sometimes diverted from the notch plane in the tested OPA specimens and followed bedding planes (see Figure 8). Thus, the fracture energy was dissipated in both the cracks: the parallel-to-notch crack and the paralell-to-bedding crack. The specimens were divided into two groups, depending on the normalized load at peak P_{p}^{*}, equal to the ratio between the peak load P_{p} and the specimen thickness S: specimens in which P_{p}^{*} was greater than 25N/mm, and specimens in which P_{p}^{*} was less than 25N/mm. It was observed that the parallel-to-bedding crack was less pronounced in the first group of specimens, therefore, it was assumed, for these specimens that all the fracture energy dissipated along the parallel-to-notch crack. Only nine specimens pertained to this group; the related test results were utilized to assess the parallel-to-bedding FM parameters (the 'selected' specimens in what follows). The inference of parallel-to-bedding FM parameters from the P vs. CMOD plots was deemed unrealistic for the remaining 13 specimens and they were therefore rejected.

a

b

c

d

Figure 9: Beam tests on the OPA; a, b, c and d refer to specimens P22, P23, P24 and P25, respectively

As previously mentioned in Section 4, in anisotropic materials the direction of crack propagation

may occur along a plane different to the planes on which the maximum circumferential stress is active, therefore the direction may be different than in the case of isotropic material. This is also evident from the results of conventional beam tests carried out on OPA specimens P22, P23, P24 and P25. They were prepared with a notch, and a bending load was applied along the notch plane. As can be seen in Figure 9, slanted cracks propagated along a bedding plane instead of along the vertical plane of the notch and they did not start from the notch except for P22, but rather from other intrinsic but unknown defects on the specimen surface. The fracture planes were clearly identified with layers of different mineralogical composition. These tests were performed in order to acquire preliminary information on the geomaterial and an order of magnitude of the mechanical resistance; strain records were not available, therefore these tests were considered useless for the determination of FM parameters.

specimen	P_p[N]	$CMOD_p$[μm]	η_p[μm]	P_p^*[N/mm]
B0302	1600	23	370	35.7
B1906	1827	14	319	38.6
B1907	1400	48	228	25.4
B1910	1231	84	236	28.6
B1911	1314	15	244	30.5
B1912	1573	14	374	41.5
B1913	1428	44	272	37.6
B1917	1986	20	353	46.1
B1918	1069	47	195	26.1

Table 2: Results obtained from the selected specimens in terms of P_p, $CMOD_p$, η_p, P_p^* (load, CMOD, deflection and normalized load at peak, respectively)

Given the variation in specimen thickness S, the normalized load P^* (equal to P/S) was considered together with P for comparison purposes with the numerical analyses. The results of the tests on the selected specimens in terms of load P, CMOD, normalized load P^* and deflection at peak η_p, are reported in Table 2.

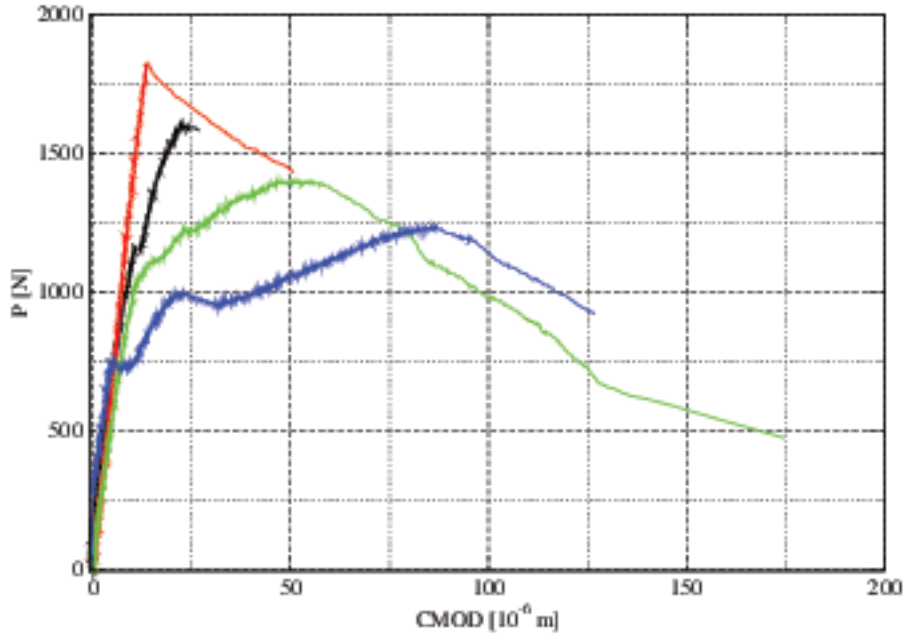

Figure 10: Plot of P vs. CMOD for specimens B0302, B1906, B1907, B1910

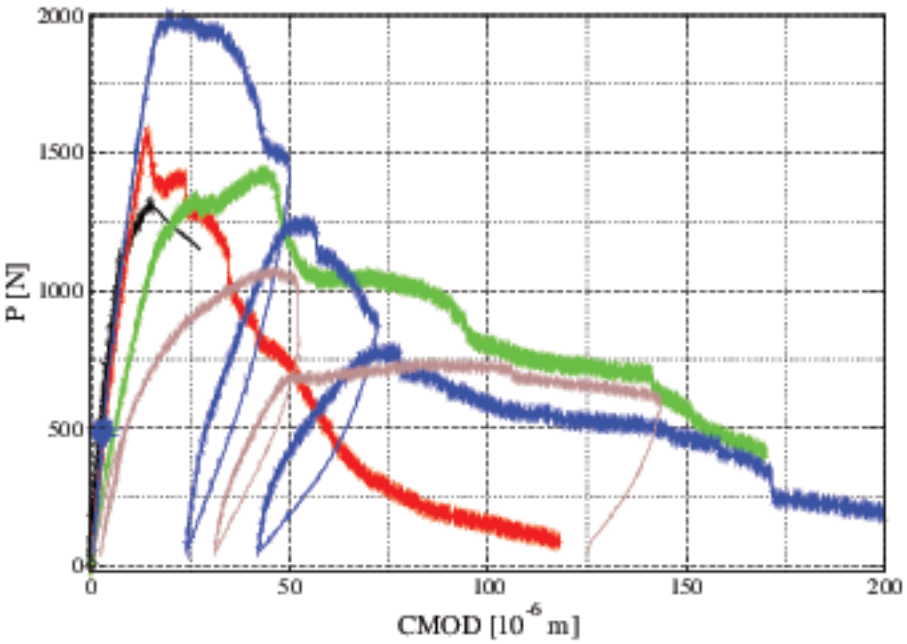

Figure 11: Plot of P vs. CMOD for specimens B1911, B1912, B1913, B1917 and B1918

The P vs. CMOD plots are reported in Figure 10 for specimens B0302, B1906, B1907, B1910 and in Figure 11 for specimens B1911, B1912, B1913, B1917 and B1918 (selected specimens).

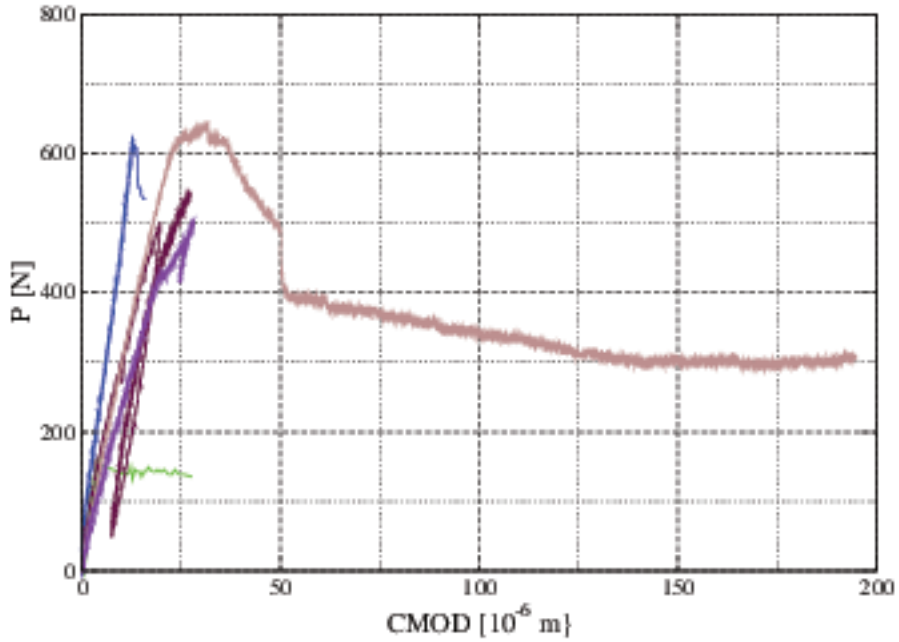

Figure 12: Plot of P vs. CMOD for the specimens B0203, B0305, B1908, B1915, B1921, B1909

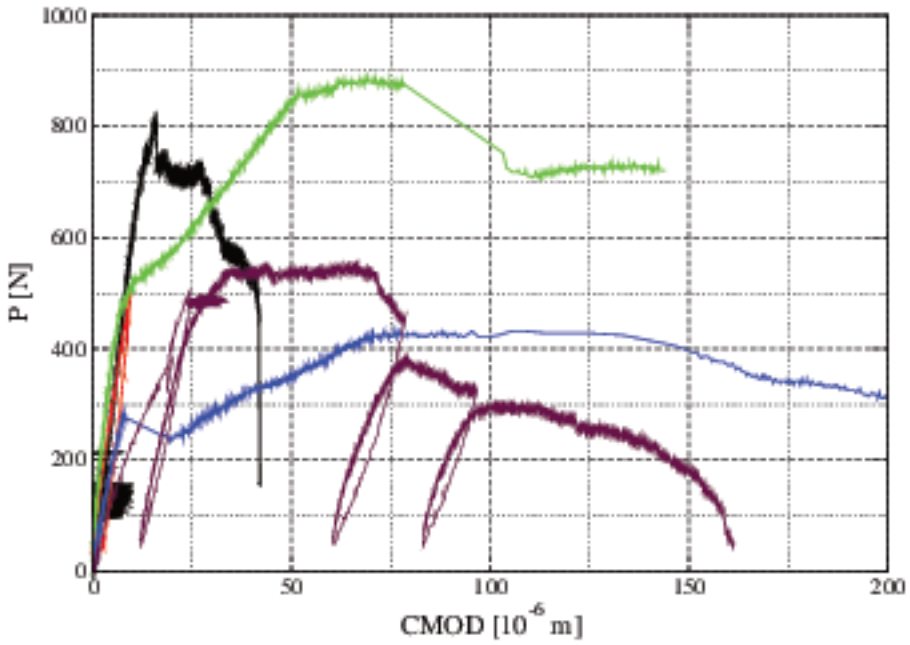

Figure 13: Plot of P vs. CMOD for specimens B1916, B1919, B0201, B0304, B1920

As far as the remaining specimens are concerned, the P vs. CMOD plots are reported in Figure 12 for specimens B0203, B0305, B1908, B1915, B1921, B1909 and in Figure 13 for specimens B1916, B1919, B0201, B0304, B1920 (CMOD was not recorded for specimens B0104 and B0105).

6 Interpretation of the fracture mechanics tests

6.1 NLFM analysis

A three-dimensional FEM NLFM model, in which the anisotropy is explicitly included, was set up to simulate the SCB-tests and derive the FM parameters. The commercial FEM code Abaqus (Dassault System Simulia Corp. (2010)) was used as the solver.

In such a model, the non-linear zone FPZ localizes in a very narrow band, while the material outside this band retains a linear behaviour. As previously mentioned, the CCM represents the narrow band as an extension of the real crack, and it is called *fictitious crack*. Although it is damaged, the material in this zone is still able to transfer stresses that are decreasing functions of the displacement discontinuity.

The model setup required definition of both the transversely isotropic linear elastic properties of the undamaged zone and of the properties of the fictitious crack. It was assumed, in the analysis, that the FPZ starts from the notch and propagates along the vertical symmetry plane of the specimen.

As far as the elastic properties are concerned, if the material is symmetric with respect to axis 3 (transverse isotropic material), the stress-strain relationship is:

$$\begin{Bmatrix} \varepsilon_1 \\ \varepsilon_2 \\ \varepsilon_3 \\ \gamma_{12} \\ \gamma_{13} \\ \gamma_{23} \end{Bmatrix} = \begin{Bmatrix} C_{11} & C_{12} & C_{13} & 0 & 0 & 0 \\ C_{12} & C_{11} & C_{13} & 0 & 0 & 0 \\ C_{13} & C_{13} & C_{33} & 0 & 0 & 0 \\ 0 & 0 & 0 & 2(C_{11}-C_{12}) & 0 & 0 \\ 0 & 0 & 0 & 0 & C_{55} & 0 \\ 0 & 0 & 0 & 0 & 0 & C_{55} \end{Bmatrix} \begin{Bmatrix} \sigma_1 \\ \sigma_2 \\ \sigma_3 \\ \tau_{12} \\ \tau_{13} \\ \tau_{23} \end{Bmatrix} \tag{2}$$

where the stresses are positive if they are tensile (convention used in Abaqus) and coefficients C_{ij} are related to five independent parameters E_1, E_3, ν_{12}, ν_{13} and G_{13} as follows:

$$C_{11} = \frac{1}{E_1},\ C_{12} = -\frac{\nu_{12}}{E_1} = -\frac{\nu_{21}}{E_2},\ C_{13} = -\frac{\nu_{13}}{E_1} = -\frac{\nu_{31}}{E_3},\ C_{33} = \frac{1}{E_3},\ C_{55} = \frac{1}{G_{13}} \tag{3}$$

The values of E_1, E_3, ν_{12}, ν_{13} and G_{13} used in the numerical simulations are reported In Table 3. These values are taken from Bock (2001).

E_1 [GPa]	E_3 [GPa]	ν_{12} [-]	ν_{13} [-]	G_{13} [GPa]
10	4	0.33	0.24	1.2

Table 3: Elastic material properties

As far as the properties of FPZ are concerned, the residual (cohesive) normal stress σ_n decreases with w_n. The displacement discontinuity vector w has three components in three dimensions: w_n normal to the crack plane while w_{t1}, w_{t2} are parallel to it. Due to symmetry, w_{t1} and w_{t2} are nil. The tangential stresses τ_1 and τ_2, parallel to w_{t1} and w_{t2} are also nil.

The stress normal to the plane of the crack, σ_n inside the FPZ is a function of normal-to-crack displacement discontinuity component w_n through the following law (Cornelissen et al, 1986):

$$\frac{\sigma_n}{f_{t\|b}} = \left[1 - \frac{1-\exp(-\alpha\, w_n/w_{m\|b})}{1-\exp(-\alpha)}\right] \tag{4}$$

that is valid for $w_n > w_{m\|b}$, where w_m is the critical value for w_n and α is a shape factor.

No stress transfer occurs between the crack walls for $w_n \geq w_m$. In the following analysis, α is kept equal to 5. Equation 4 is reported for such a value of α in Figure 14. The shape of the function is typical of concrete and stiff geomaterials. The integral of the $\sigma_n(w_n)$ is the Mode-I fracture energy G_f.

Figure 15 shows the boundary and loading conditions of the model. A downward displacement is applied to the upper part of the specimen in order to simulate the effect of the loading device, which is assumed to be infinitely rigid. Notch width b_0 is assumed negligible. The dip vector of the bedding planes is inclined 45° with respect to the horizontal plane and lies in the plane of the notch. Figure 16 shows the used FEM mesh in which type-C3D4 4-node tetrahedral elements have been utilized.

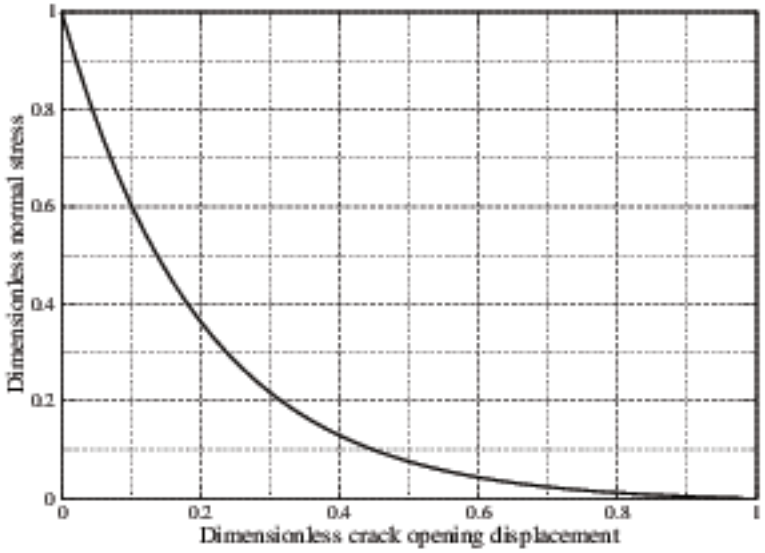

Figure 14: Softening law for α=5 from Eq. 4

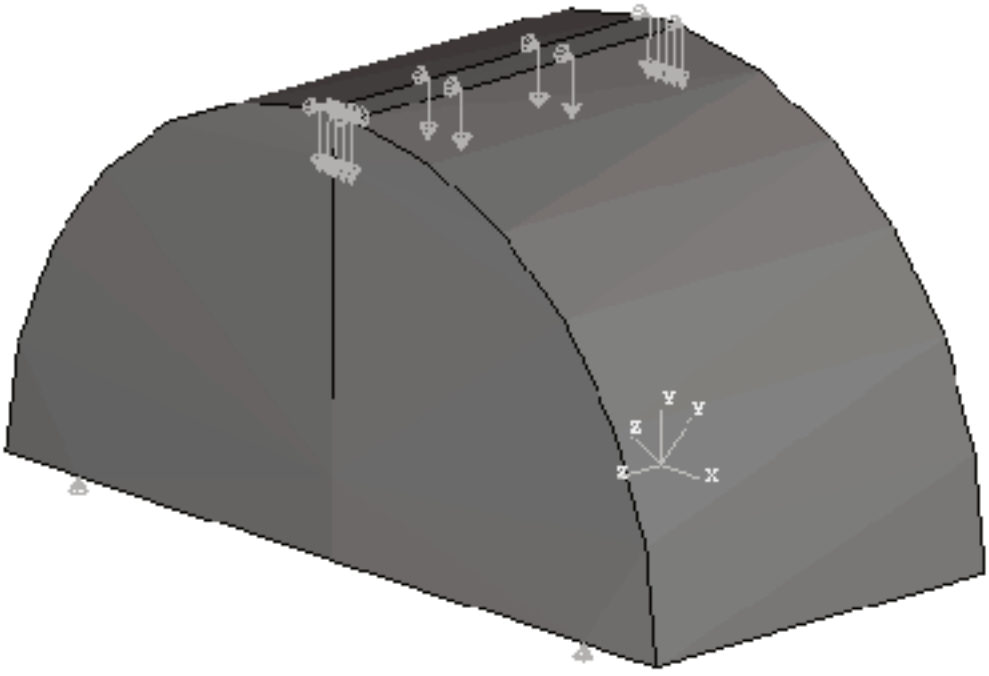

Figure 15: Axonometric view of the model with indications of the boundary conditions

Since the shape of the softening law is predefined (α=5, a typical value for concrete-like materials), just two parameters ($w_{\mathrm{m}\|\mathrm{b}}$ and $f_{\mathrm{t}\|\mathrm{b}}$) have to be determined through the back-simulation of the observed crack growth response. The baseline of the parallel-to-bedding FM properties is reported in Table 4 in which the value of $f_{\mathrm{t}\|\mathrm{b}}$ is taken from Bock (2001). The results obtained using these

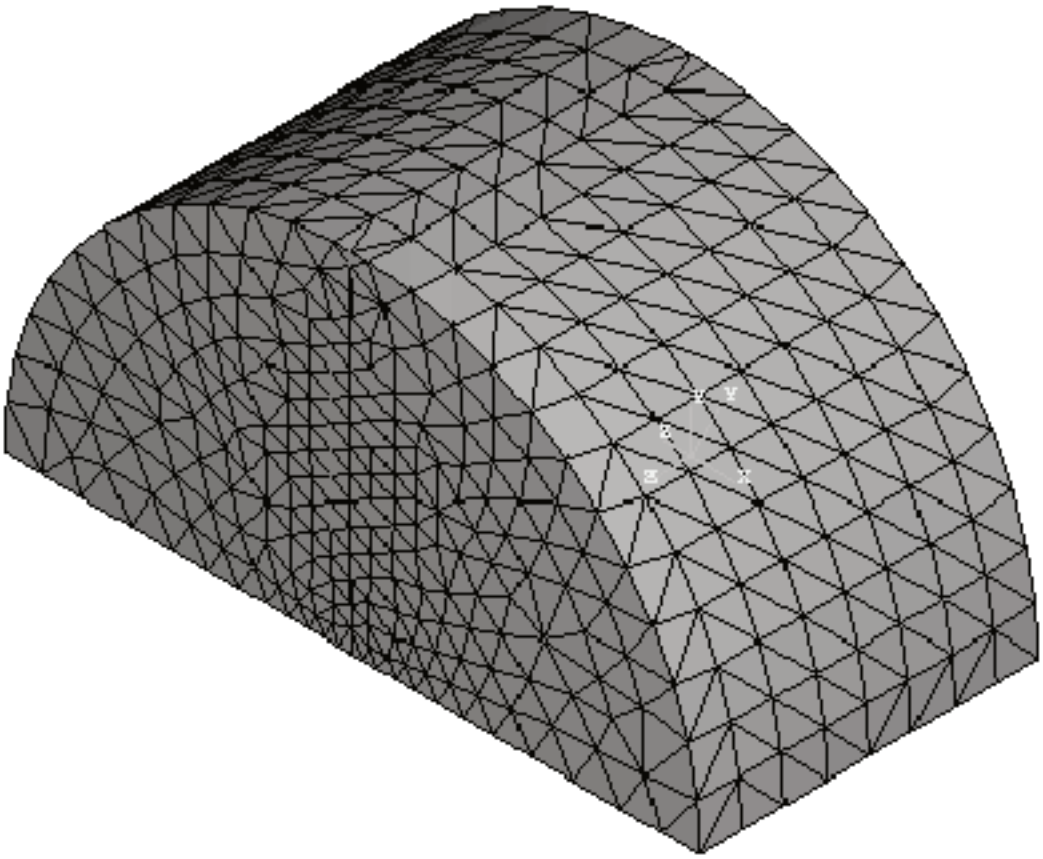

Figure 16: Finite element mesh

$f_{t\|\|b}$[MPa]	$G_{f\|\|b}$[N/m]	$w_{m\|\|b}$[mm]
2	38	0.1

Table 4: Parallel-to-bedding Fracture Mechanics properties

parameters are comparable with the experimental results shown in Figures 10 and 11. In order to evaluate the variability of the mechanical response a sensitivity analysis was also carried out.

6.2 CCM numerical results

	$f_{t\|\|b}$ [MPa]	$w_{m\|\|b}$ [mm]
baseline	2	0.1
FTMWMM	1.5	0.075
FTMWMP	1.5	0.125
FTPWMM	2.5	0.075
FTPWMP	2.5	0.125

Table 5: Input data for the sensitivity analysis

First, it is worth mentioning that, as a consequence of the transverse isotropy and orientation of the notch plane with respect to the bedding, the CMOD is not uniform along the specimen thickness (see Figure 17). CMOD was evaluated at the specimen center, as in the experimental setup, for the comparison with the experimental results.

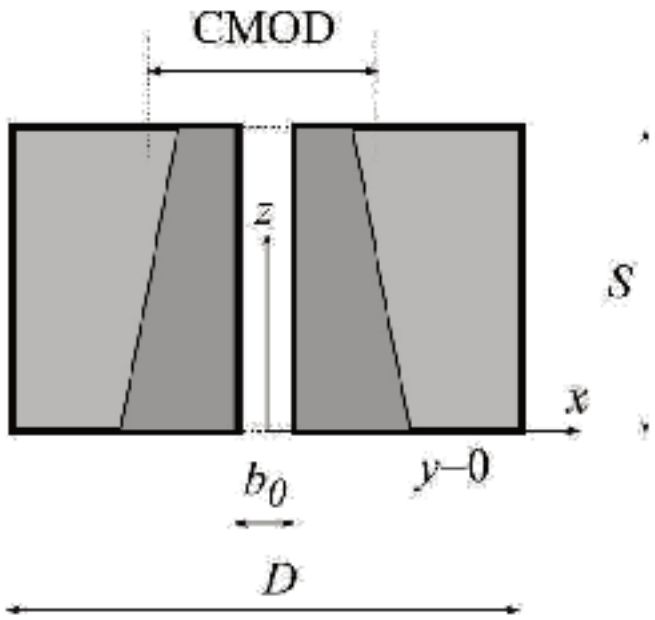

Figure 17: View from the bottom of the specimen with CMOD distribution along the notch

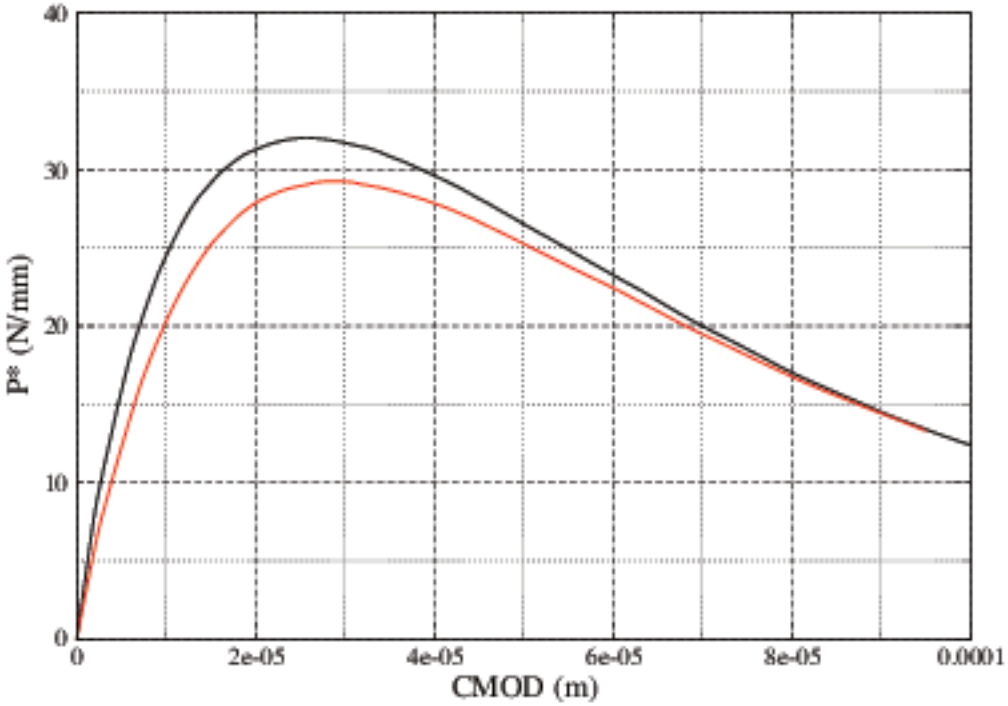

Figure 18: Plot of P^* vs. CMOD: upper curve for notch depth a_0 5.4mm, lower curve for notch depth a_0 7.3mm

Before undertaking a sensitivity analysis of the mechanical response with respect to the FM parameters, two runs of the model with a_0 equal to 5.3 and 7.3mm were carried out, given the variability of the notch depth a_0 in the experiments (extreme values of specimens from borehole B19 in Table 1), Figure 18 shows the vertical load per unit specimen thickness plotted against CMOD for both cases. It is apparent that, in the chosen range of a_0, the notch depth does not influence the response, thus,

in what follows, an average depth value of 6mm was considered.

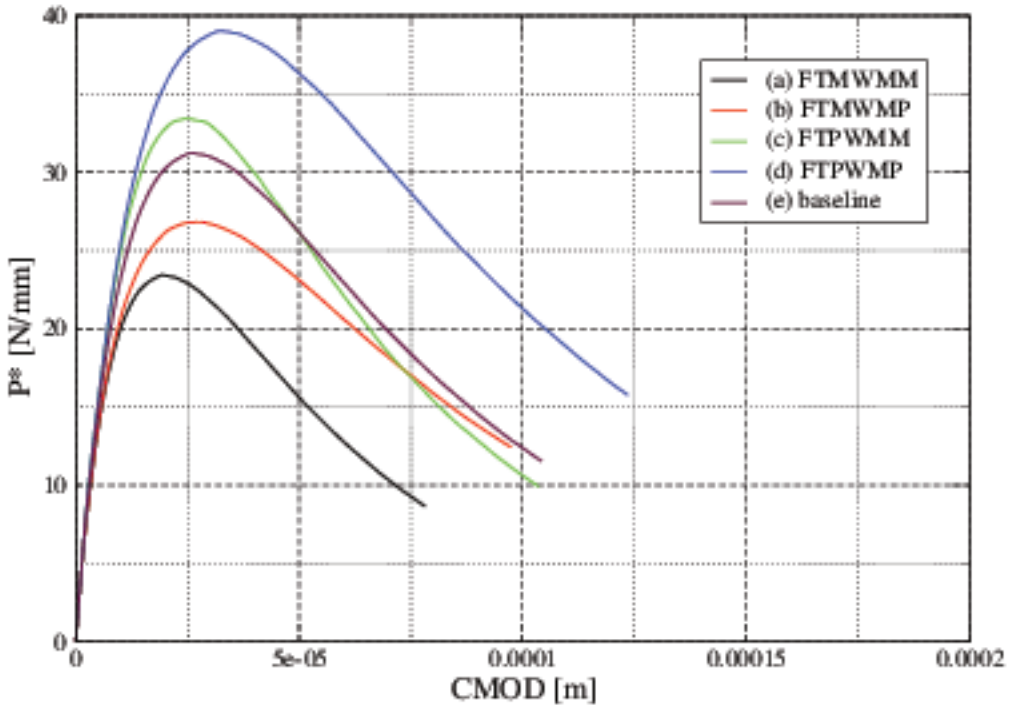

Figure 19: Sensitivity of P^* vs. CMOD plot to $f_{t\|b}$ and $w_{m\|b}$; given the related baseline values $f^*_{t\|b}$ and $w^*_{m\|b}$, the plots refer to the following combinations: (a) FTMWMM, $75\%f^*_{t\|b}$, $75\%w^*_{m\|b}$; (b) FTMWMP, $75\%f^*_{t\|b}$, $125\%w^*_{m\|b}$; (c) FTPWMM, $125\%f^*_{t\|b}$, $75\%w^*_{m\|b}$; (d) FTPWMP, $125\%f^*_{t\|b}$, $125\%w^*_{m\|b}$; (e) baseline values

The sensitivity of the response to $f_{t\|b}$ and $w_{m\|b}$ was evaluated by running four models, each one with a specific couple $f_{t\|b}$, $w_{m\|b}$ (see Table 5). The effect of a $\pm 25\%$ perturbation from the baseline values was investigated with these models. In Figure 19 the numerical normalized load P^* vs. CMOD plots for all the models of Table 5 are reported. The numerical peak values P^*_p and $CMOD_p$ cover the ranges of the corresponding experimental values of Table 2, therefore it can be assumed that OPA $f_{t\|b}$ and $w_{m\|b}$ have average values coinciding with the baseline values and deviations of around 25%.

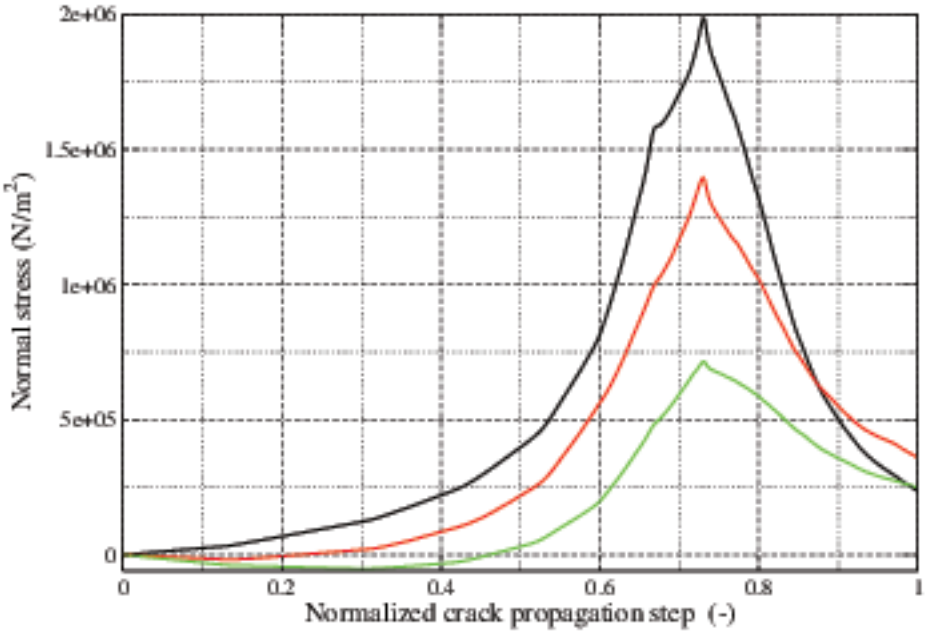

Figure 20: Normal stresses at a fixed location ($x = 0$, $y = 0.022$m, $z = 0.02$m) for a notch depth a_0 of 7.3mm plotted against the normalized crack propagation step; upper curve σ_x, curve in the middle σ_y, lower curve σ_z

Close to the crack tip, the tangential stress acting on the coordinates planes is negligible, therefore the corresponding normal stress acting on bedding plane σ_n can be assumed as the mean of σ_{yy} and σ_{zz}. As shown in Figure 20, in which the normal stresses are plotted against the advancement of the crack (normalized to the crack length at the end of the simulation), σ_n (tensile) can be larger than normal-to-bedding tensile strength $f_{t,\perp b}$, assumed equal to 1MPa (Bock (2001)), thus a parallel-to-bedding crack may superpose on the initial parallel-to-notch crack, as shown in Figure 8.

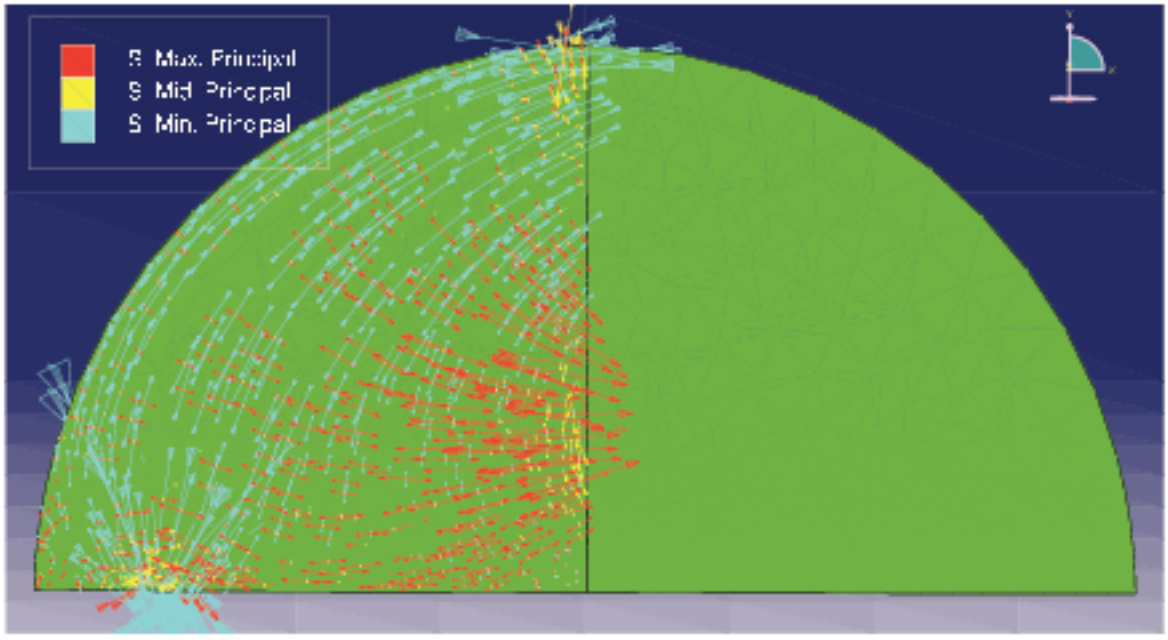

Figure 21: Principal stresses for a vertical cross section

The concentration of tensile stresses close to the notch is shown in Figure 21, where the arrows indicate the principal stresses.

Figure 18 shows that CMOD, at peak load, is in the $20 \div 30\mu$ range, therefore, the displacement discontinuity at the real crack tip is smaller than the limit value $w_{\mathrm{m}\|\mathrm{b}}$ of 100μ (see Table 4), and the FPZ is not completely developed. Since the quasi-brittle material is characterized by an internal length ($w_{\mathrm{m}\|\mathrm{b}}$), the relative length of the process zone reduces with an increase in the structural size. As a consequence, a specific size value exists for which the length of the process zone is negligible in comparison to core diameter D.

7 Concluding remarks

In this paper, the results of SCB tests on OPA are illustrated and interpreted in the framework of NLFM, and the corresponding FM parameters for the bedding direction (i.e. fracture plane normal-to-bedding) are deduced.

It is well known that a large scatter in the experimental peak loads can be expected in tests executed on specimens without notches. Instead, when a notch exists, the crack is usually expected to initiate from the notch itself, irrespective of the defects in its vicinity. For this reason, and particularly for SCB tests, this scatter is supposed to reduce. However, in the tests documented herein, ad additional parallel-to-bedding crack frequently appeared. This crack led to a further dissipation of energy, and, as a consequence, the peak load was different from the value that could be obtained in case of a single crack.

Since this second type of crack is likely to develop along a certain number of bedding planes, the random distribution of defects has played a central role, that is exactly what happens on a specimen without a notch, and, as a consequence, a large scatter of the experimental peak loads has been shown. In some of the tests, the second crack prevailed, and the peak load resulted to be very low, thus the related results were disregarded. The remaining tests were then used for the interpretation. The scatter of the peak load in these selected tests should therefore be ascribed to both the bias due to the emerging altough not prevailing supplementary crack and the intrinsic heterogeneity of the material.

The superposition of the two damage mechanisms and the role of anisotropy should be taken into account in future studies, in view of a more detailed understanding of the crack growth that occurs within the EDZ in the OPA. The SCB test method proved useful to extricate one mechanism from the other, because the crack is relatively forced to follow the plane of the notch.

Ranges of the parallel-to-bedding FM parameters were defined through a sensitivity analysis and using a numerical NLFM model. It has been shown that FEM can be efficiently used for the solution of a NLFM model; in fact the experimental results with CCM were replicated with an acceptable degree of approximation.

8 Acknowledgements

The authors would like to thank the Swiss Nuclear Safety Inspectorate ENSI and Dr. Erik Frank who financially supported the EZ-B research project. Thanks are also due to the partners who contributed to this project, and especially Salina Yong, Peter Kaiser and Florian Amann for the exchange of fruitful ideas and discussions.

References

Amann F, Button E, Evans K, Gischig V, Bl umel M (2011) Experimental study of the brittle behavior of clay shale in rapid unconfined compression. Rock Mechanics and Rock Engineering 4(44):415–430

Barenblatt G (1959) The formation of equilibrium cracks during brittle fracture: general ideas and hypotheses. Journal of Applied Mathematics and Mechanics 23(3):622–636

Barpi F, Valente S (2010) The cohesive frictional crack model applied to the analysis of the dam-foundation joint. Engineering Fracture Mechanics 77:2182–2191, Elsevier Science Ltd. (Great Britain)

Bocca P, Carpinteri A, Valente S (1991) Mixed-mode fracture of concrete. International Journal of Solids and Structures 27:1139–1153

Bock H (2001) RA experiments rock mechanics analyses and synthesis: data report on rock mechanics. Tech. rep., Mont Terri Project, Tech. Report 2000–02

Buczek M, Herakovich C (1985) A normal stress criterion for crack extension direction in orthotropic materials. Journal of Composite Materials 19:44–553

Carter B, Lajtai E, Yuan Y (1992) Tensile fracture from circular cavities loaded in compression. International Journal of Fracture 57:221–236

Chandler N (2004) Developing tools for excavation design at Canada's Underground Research Laboratory. International Journal of Rock Mechanics and Mining Sciences 41:1229–1249

Corkum A, Martin C (2007) The mechanical behaviour of weak mudstone (Opalinus Clay) at low stresses. International Journal of Rock Mechanics and Mining Sciences 44:196–209

Cornelissen H, Hordijk D, Reinhardt H (1986) Experimental determination of crack softening characteristics of normal and lightweight concrete. Heron 31:45–56

Dassault System Simulia Corp (2010) ABAQUS release 6.10. Tech. rep., Providence, RI

Diederichs M (2007) The 2003 CGS Geocolloquium Address: Damage and spalling prediction criteria for deep tunnelling. Canadian Geotechnical Journal 44(9):108–1116

Dugdale D (1960) Yielding of steel sheets containing slits. Journal of Mechanics and Physics of Solids 8:100–114

Ewy RT, Cook NGW (1990) Deformation and fracture around cylindrical openings in rock - i. Observations and analysis of deformations. Int J Rock Mech Min Sci Geomech Abstr 27(5):387–407

Gaucher E, Fernandez A, Waber H (2003) Rock and mineral characterisation of the Opalinus Clay Formation. Tech. rep., Reports of the Federal Office for Water and Geology, Geology Series No. 5

Germanovich L, Dyskin A (2000) Fracture mechanisms and instability of openings in compression. International Journal of Rock Mechanics and Mining Sciences (37):263–284

Hajiabdolmajid V, Kaiser P, Martin C (2002) Modelling brittle failure of rock. International Journal of Rock Mechanics & Mining Sciences 39:731–741

Hillerborg A, Modeer M, Petersson P (1976) Analysis of crack formation and crack growth in concrete by means of fracture mechanics and finite elements. Cement and Concrete Research 6:773–782

Hudson J, Backstrom A, Rutqvist J, Jing L, Backers T, Chijimatsu M, Christiansson R, Feng X, Kobayashi A, Koyama T, Lee H, Neretnieks I, Pan P, Rinne M, Shen B (2009) Characterising and modelling the excavation damaged zone in crystalline rock in the context of radioactive waste disposal. Environmental Geology 6(57):1275–1297

Loew S, Barla G, Diederichs M (2010) Engineering geology of alpine tunnels: past, present and future. In: Williams A, Pinches C, Chin C, McMorran T, Massey C (eds) Geologically Active, Proceedings 11th IAEG Congress, Auckland, NZ, CRC Press, pp 201–254

Martin C, Lanyon G (2001) EDZ in clay shale: Mont Terri. Tech. Rep. 2001-01, Mont Terri Project

Mazurek M (2002) Mineralogical composition of Opalinus Clay at Mont Terri – A laboratory intercomparison. Mont Terri internal unpublished report

Nussbaum C, Bossart P, Amann F, Aubourg C (2011) Analysis of tectonic structures and excavation induced fractures in the Opalinus Clay, Mont Terri underground rock laboratory (Switzerland). Swiss Journal of Geosciences (104):187–210

Saouma V, Ayari M, Leavell D (1987) Mixed mode crack propagation in homogeneous anisotropic solids. Engineering Fracture Mechanics 27:171–184

Thury M, Bossart P (1999) Mont Terri rock laboratory: results of the hydrogeological, geochemical and geotechnical experiments performed in 1996 and 1997. Tech. Rep. Geological reports No. 23, Swiss National Hydrological and Geological Survey, Bern-Ittigen

Wetzel A, Allia V (2003) Der Opalinuston in der Nordschweiz: Lithologie und Ablagerungsgeschichte. Eclogae Geologicae Helvetiae (96):451–469

Yong S (2007) A three-dimensional analysis of excavation-induced perturbations in the Opalinus Clay at the Mont Terri Rock Laboratory. PhD thesis, Swiss Federal Institute of Technology (Zurich)

Yong S, Loew S, Fidelibus C, Frank E, Lemy F, Schuster K (2006) Induced fracturing in the Opalinus Clay: An integrated field experiment. In: Proc. Asian Rock Mechanics Symposium (ARMS 2006) Singapore

Yong S, Kaiser P, Loew S (2010) Influence of tectonic sheras on tunnel-induced fracturing. International Journal of Rock Mechanics & Mining Sciences 47:894–907